



<http://www.diva-portal.org>

This is the published version of a paper published in *Journal of the Electrochemical Society*.

Citation for the original published paper (version of record):

Benavente Araoz, F A. (2020)

Effect of Partial Cycling of NCA/Graphite Cylindrical Cells in Different SOC Intervals

Journal of the Electrochemical Society, 167(040529)

<https://doi.org/10.1149/1945-7111/ab78fd>

Access to the published version may require subscription.

N.B. When citing this work, cite the original published paper.

Permanent link to this version:

<http://urn.kb.se/resolve?urn=urn:nbn:se:kth:diva-295636>

OPEN ACCESS

Effect of Partial Cycling of NCA/Graphite Cylindrical Cells in Different SOC Intervals

To cite this article: Fabian Benavente-Araoz *et al* 2020 *J. Electrochem. Soc.* **167** 040529

View the [article online](#) for updates and enhancements.



Effect of Partial Cycling of NCA/Graphite Cylindrical Cells in Different SOC Intervals

Fabian Benavente-Araoz,^{1,2,z} Maria Varini,¹ Anders Lundblad,^{3,*} Saúl Cabrera,² and Göran Lindbergh¹

¹Department of Chemical Engineering, Applied Electrochemistry, KTH Royal Institute of Technology, Stockholm, Sweden

²Instituto de Investigaciones Químicas, UMSA Universidad Mayor de San Andrés, La Paz, Bolivia

³Division of Safety and Transport/Electronics, RISE, Research Institutes of Sweden, SE-50462 Borås, Sweden

A quasi-realistic aging test of NCA/graphite lithium-ion 18650 cylindrical cells is performed during a long-term low c-rate cycling and using a new protocol for testing and studying the aging. This to emulate a characteristic charge/discharge profile of off-grid PV-battery systems. The cells were partially cycled at four different cut-off voltages and two state of charge ranges (Δ SOC) for 1000 and 700 cycles over 24 months. Differential voltage analysis shows that a combination of loss of active material (LAM) and loss of lithium inventory (LLI) are the causes of capacity loss. Cells cycled with high cut-off voltages and wide Δ SOC (20% to 95%) were severely affected by material degradation and electrode shift. High cut-off voltage and narrow Δ SOC (65% to 95%) caused greater electrode degradation but negligible cell unbalance. Cell impedance is observed to increase in both cells. Cells cycled with middle to low cut-off voltages and narrow Δ SOC (35%–65% and 20% to 50%) had comparable degradation rates to calendar-aged cells. Cycling NCA/graphite cells with low c-rate and high cut-off voltages will degrade the electrode in the same way high c-rate would do. However, low c-rate at low and middle cut-off voltages greatly decrease cell degradation compared to similar conditions at middle to high c-rate, therefore increasing battery lifetime.

© 2020 The Author(s). Published on behalf of The Electrochemical Society by IOP Publishing Limited. This is an open access article distributed under the terms of the Creative Commons Attribution 4.0 License (CC BY, <http://creativecommons.org/licenses/by/4.0/>), which permits unrestricted reuse of the work in any medium, provided the original work is properly cited. [DOI: 10.1149/1945-7111/ab78fd]



Manuscript submitted November 15, 2019; revised manuscript received January 27, 2020. Published March 12, 2020. This was Paper 212 presented at the Cancun, Mexico, Meeting of the Society, September 30–October 4, 2018.

Lithium-ion batteries (LIBs) have tremendous potential to become a key component in the electrification of disperse rural areas where conventional electrification infrastructure is too expensive to be implemented. This is the case for off-grid PV-battery systems operation, where relatively low currents are needed to fulfill the load and to charge the battery, as we observed in a previous work.¹ LiNiCoAlO₂ (NCA) as active material in the positive electrode is currently used in transportation applications as well as stationary systems, because of its potential for high energy density and convenient cost/energy storage ratio.^{2–5} However, capacity fade, power loss, impedance increase, and particle cracking are aging mechanisms observed under different operating conditions.^{6–10} It was reported that capacity loss in NCA/graphite cells cycled in wide state of charge ranges (Δ SOC) is caused by micro-crack generation in NCA particles.⁵ Watanabe et al.,⁶ showed that cycling NCA/graphite cells with 2 C/1 C current rates and restricted Δ SOC can suppress the generation of micro-cracks in the NCA electrode. They obtained similar capacity fade rates for three different Δ SOC (e.g. 100%–40%, 90%–30%, 60%–0%). Bloom et al. have studied calendar and cycle aging of NCA/graphite cells, where they used differential voltage analysis (DVA) to identify main causes of capacity loss, pointing mainly to side reactions in the graphite electrode.^{7,11} Watanabe et al. tested cycling of cylindrical full cells at four partial depth of discharge thresholds and 1 C current rate; they found that micro-cracks at NCA particle surface were the main cause of capacity fade and increased cell resistance.¹² Aging effects on NCA/graphite cells when cycled at high Δ SOC are related to surface phase transitions of NCA particles and micro-crack formation in their surface, increasing the charge transfer resistance and reducing the overall cell performance.^{6,9,10,12–17} In addition, DVA analysis was also used to evaluate calendar aging of NCA/graphite cells. Keil et al.,^{18,19} found that calendar aging at high Δ SOC causes capacity fade mainly as side reactions in the graphite electrode related to electrolyte reduction and passivation layer growth. Although various authors have studied the aging mechanisms of both NCA and graphite electrodes, most of the research works use

accelerated aging techniques which are focused on electric vehicle (xEV) operating conditions, while research studies oriented to stationary storage applications are still scarce. Battery aging protocols commonly used for xEV applications are not necessarily the same as those used for stationary energy storage systems. The current at which charge/discharge cycles are performed constitutes the main difference. Additionally, the Δ SOC at which the battery is cycled vary considerably.

Although there are plenty of scientific publications studying aging of NCA/graphite cells in various geometries, most of the aging conditions use middle (C/2 to 1 C)^{9,16,20–23} to high (2 C to 20 C)^{2,20–22} current rates. Smith et al.,²³ propose the study of low current rate impact on LCO/graphite cells, although not studying the cut-off voltage effect and based on a different chemistry. High c-rate studies can lead to unrealistic predictions of degradation in the case of low c-rate applications off-grid systems.

In contrast to studies evaluating aging under medium and high c-rate cycling,^{24,25} this work intends to address the effects of long-term low c-rate cycling and Δ SOC on capacity fade and impedance increase in commercial NCA/graphite cylindrical cells. The observed results give us better understanding of the aging mechanisms affecting each electrode for off-grid stationary energy storage applications.

The paper is organized as follows: Experimental starts by describing the type of cell, cycling, and characterization parameters used, along with techniques and equipment. The results and discussion firstly present characterization data from the full-cell cycling and continue with half-cell *post-mortem* characterization. Finally, the conclusions are presented.

Experimental

Cylindrical cells and aging protocols.—Commercial high-capacity 18650 cylindrical cells (2.5Ah, INR18650-25R, Samsung SDI) containing LiNiCoAlO₂ (NCA) as positive electrode and graphite as negative electrode were used in this study. The manufacturer specifications for the cells are presented in Table I.

In order to investigate the aging effects of partial cycling at different state of charge ranges (Δ SOC) and low c-rates, cells were cycled following the procedures and conditions presented in

*Electrochemical Society Member.

^zE-mail: faba@kth.se

Table I. Cell specifications (INR18650-25R).

Item	Specification
Nominal discharge capacity	2,500 mAh
Charging voltage	4.2 ± 0.05 V
Nominal voltage	3.6 V
Charging method	CCCV, 125 mA cut-off
Charging current	Standard charge: 1.25 A Rapid charge: 4 A (100 mA cut-off)
Max. discharge current	20 A (at 25 °C), 60% at 250 cycle
Discharge cut-off voltage	2.5 V
Cell weight	45.0 g (max)
Operating temperature	Charge: 0. To 50 °C Discharge: -20 to 75 °C
Storage temperature	1.5 year -30 °C-25 °C 3 months -30 °C-45 °C 1 month -30 °C-60 °C

Table II. Cells were cycled in four different Δ SOC: 65%–95%, 35%–65%, 20%–50%, and 20%–95% which are represented as A, B, C, and D, respectively. End of test (EOT) was set when cells A, B, and C reached 1,000 partial cycles and cell D reached 700 partial cycles. The Δ SOC ranges were selected considering the most common battery operation scenarios observed in small off-grid PV/battery systems.^{1,26} Calendar-aged cells are used as non-cycled reference to further compare them to the cycle-aged cells. The calendar-aged cells were stored at 25 °C and 50% SOC for the whole testing period. A NEWARE BTS-4000 battery testing system was used for cycling the cells at four different Δ SOC. All test procedures were performed inside a temperature-controlled climate chamber, Friocell 111 Comfort MMM Lab, set at 25 °C. A duplicate cell was used for each aging condition to ensure the reproducibility of the obtained test parameters.

Slow discharge capacity and electrochemical impedance spectroscopy (EIS) tests were performed on each cell after approximately every 100 partial cycles along with the calendar-aged cells. Before slow discharge capacity characterization, cycle-aged and calendar-aged cells were fully charged to 4.2 V following the manufacturer specifications (CCCV) as shown in Table I. Then cells were fully discharged by applying constant current at C/25 rate until reaching 2.5 V. Finally, galvanostatic EIS was used to obtain the impedance spectra of each cell at 50% SOC and 25 °C. The frequency range was set between 25 mHz and 1 kHz with a 100 mA sinusoidal current perturbation. A Gamry PCI/750 galvanostat/potentiostat was used

along with a four-point connection cell holder. Due to equipment malfunction, the whole experiment was stopped for 6 months between partial cycle number 900 and 1,000. During this time, the cells were stored at 25 °C and 50% SOC.

In order to compare the capacity fade among the cycled-aged cells, despite the different Δ SOC ranges at which cells were cycled, we calculated the equivalent full cycles. Equivalent full cycles (EFC, see Eq. 1) were calculated by multiplying the number of partial cycles with the Δ SOC fraction corresponding to the Δ SOC at which the cells were cycled.

$$EFC = \text{cycles}_{\text{partial}} \times \frac{\Delta\text{SOC}_{\text{window}}}{\Delta\text{SOC}_{100\%}} \quad [1]$$

Post-cycling characterization.—After reaching the EOT mark, cycle-aged and calendar-aged cells were discharged using a CCCV protocol to 2.5 V before being disassembled in an argon-filled glove box (O_2 and H_2O <1 ppm), where cathode and anode electrodes sheets were carefully extracted from the jellyroll of each cell. Samples were punched into 28 mm diameter electrodes and used to build up half-cells with lithium metal foil as counter and reference electrode. Such samples were cleaned following the methodology from Ref. 27.

The remaining half-cell components were: Whatman glass-fiber as separator soaked with 1 M LiPF₆ in 1:1 EC/DMC electrolyte (LP40, Merck).

Ultra-low current discharge OCV curves were obtained using half-cells assembled with harvested electrodes from the aged cylindrical cells. Graphite/lithium half-cells were preconditioned running two cycles at C/10 and lithiated at C/54 between 0.002–1.5 V. Likewise, NCA/lithium half-cells were preconditioned at C/10 and delithiated at C/54 between 4.3–3 V. A Keithley 220 current source and Keithley 2700 differential multimeter controlled with LabVIEW routines were used for this purpose. Additionally, surface and morphology characterization were performed using a field emission scanning electron microscope (FE-SEM S-4800, Hitachi).

Results and Discussion

Capacity fade of cylindrical cells.—Figure 1 shows the relative full-discharge capacity of cells partially cycled at different Δ SOC as a function of the number of equivalent full cycles (EFC). The average full-discharge capacity value of two cells cycled under the same conditions is considered for each case. Relative capacity is defined as the ratio of the average capacity value of cells cycled in a

Table II. Overview of partial cycling procedures.

Aging case	Step	Parameters	Termination
65–95 SOC% Code A6595	1) Charge CCCV	$I = 280 \text{ mA}$, $V = 4.10 \text{ V}$	$t > 60 \text{ min}$ or $I < 0.01 \text{ A}$
	2) Discharge CC	$I = -320 \text{ mA}$	$V = 3.85 \text{ V}$
	3) Rest (OCP)	OCP	$t > 120 \text{ min}$
	4) # Partial Cycles	1000	
35–65 SOC% Code B3565	1) Charge CCCV	$I = 280 \text{ mA}$, $V = 3.85 \text{ V}$	$t > 60 \text{ min}$ or $I < 0.01 \text{ A}$
	2) Discharge CC	$I = -320 \text{ mA}$	$V = 3.60 \text{ V}$
	3) Rest (OCP)	OCP	$t > 120 \text{ min}$
	4) # Partial Cycles	1000	
20–50 SOC% Code C2050	1) Charge CCCV	$I = 280 \text{ mA}$, $V = 3.69 \text{ V}$	$t > 60 \text{ min}$ or $I < 0.01 \text{ A}$
	2) Discharge CC	$I = -320 \text{ mA}$	$V = 3.47 \text{ V}$
	3) Rest (OCP)	OCP	$t > 120 \text{ min}$
	4) # Partial Cycles	1000	
20–90 Δ SOC% Code D2095	1) Charge CCCV	$I = 280 \text{ mA}$, $V = 4.10 \text{ V}$	$t > 60 \text{ min}$ or $I < 0.01 \text{ A}$
	2) Discharge CC	$I = -320 \text{ mA}$	$V = 3.47 \text{ V}$
	3) Rest (OCP)	OCP	$t > 120 \text{ min}$
	4) # Partial Cycles	700	

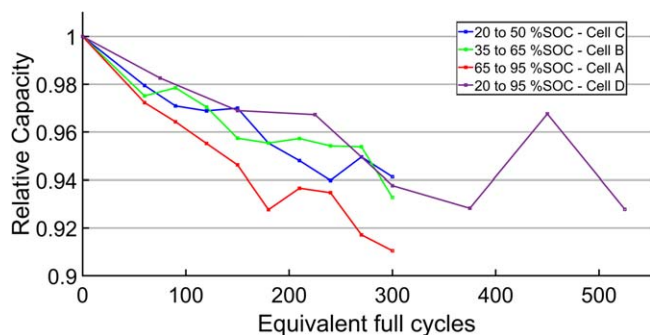


Figure 1. Relative discharge capacity as function of the number of equivalent full cycles.

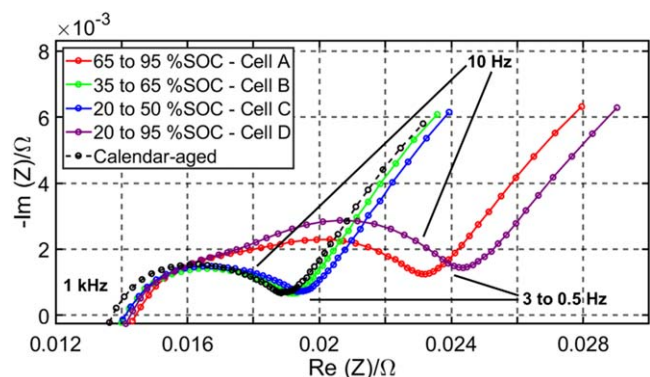


Figure 2. Impedance spectra of full-cells at the end of test for the four cycle-aged cells and calendar-aged cell as reference.

specific range to the average initial capacity values at beginning of test (BOT). In order to compare the observed capacity loss among cells, the horizontal axis represents EFC. Four different Δ SOC are described in Table III, the c-rates were adjusted to mimic a small off-grid PV-system daily operation. After 300 EFC, the discharge capacities of cells A, B, and C were reduced by 8.9, 6.7, and 5.9% from their BOT value, respectively. Cell D went through 525 EFC and its discharge capacity was reduced by 7.2%.

Although the conventional 20% capacity reduction at end of life (EOL) was not achieved, the values observed correspond to almost 24 months of testing, which in this case corresponds to the end of test (EOT). Despite that cell D was cycled for 525 EFC, the capacity loss was greatest for cell A which was cycled for only 300 EFC. Moreover, cycling the cells with middle and low cut-off voltages and narrow Δ SOC (35% to 65% and 20% to 50%) seems to reduce the capacity loss rate. The calendar-aged cell shows a capacity loss of 3.4% when EOT was reached; this value is in good agreement with literature.¹⁸ (Note: at 270 EFC for cells A, B, and C, and 450 EFC

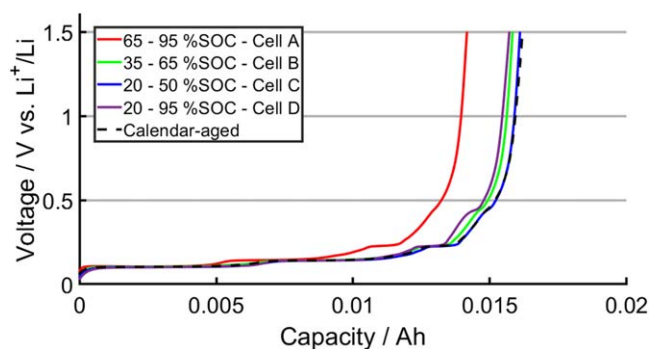


Figure 3. Discharge curves of the graphite electrode harvested from cells A, B, C, and D and calendar-aged cell (dashed line).

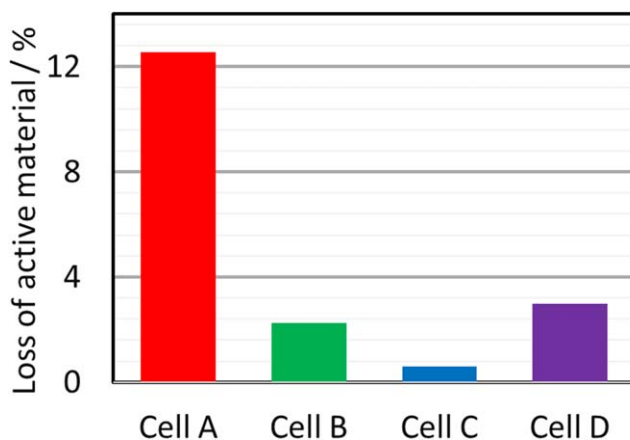


Figure 4. loss of active material percentage of graphite/lithium cycled-aged half-cells relative to calendar-aged half-cell, after partial cycling at different SOC ranges.

for cell D, due to a malfunction of the cycling equipment, the cells were stored during a period of 6 months in a temperature chamber at 25 °C and 50% SOC before restarting the cycling and characterization.)

A recovery of capacity can be observed (see Fig. 1) after 210 EFC in cell A, after 90 and 210 EFC in cell B, after 150 and 300 EFC in cell C, and after 450 EFC in cell D. This behavior was previously observed by some authors,^{28,29} and attributed to deviations from homogeneous lithium distribution and anode overhang. Although the capacity is recovered at the mentioned points, the capacity fade follows a rather constant rate until reaching EOT.

Partial cycling is considered to reduce the capacity loss in NCA/graphite cells.^{6,30} This is not the case for cells cycled at high cut-off voltages, despite the low current applied. However, when cycled with middle and low cut-off voltages, and narrow Δ SOC, the

Table III. Capacity values of commercial cells partially cycled at different SOC ranges.

Cell	SOC range (%)	V range [V]	Number of partial cycles	Number of EFC	BOL Cap. [Ah]	EOT Cap. [Ah]	Cap. fade [%]
Calendar-aged	—	—	—	—	2.49	2.41	3.2
A	95–65	4.10 3.85	1000	300	2.55	2.32	8.9
B	65–35	3.85 3.60	1000	300	2.54	2.37	6.7
C	50–20	3.69 3.47	1000	300	2.52	2.37	5.9
D	95–20	4.10 3.47	700	525	2.50	2.31	7.2

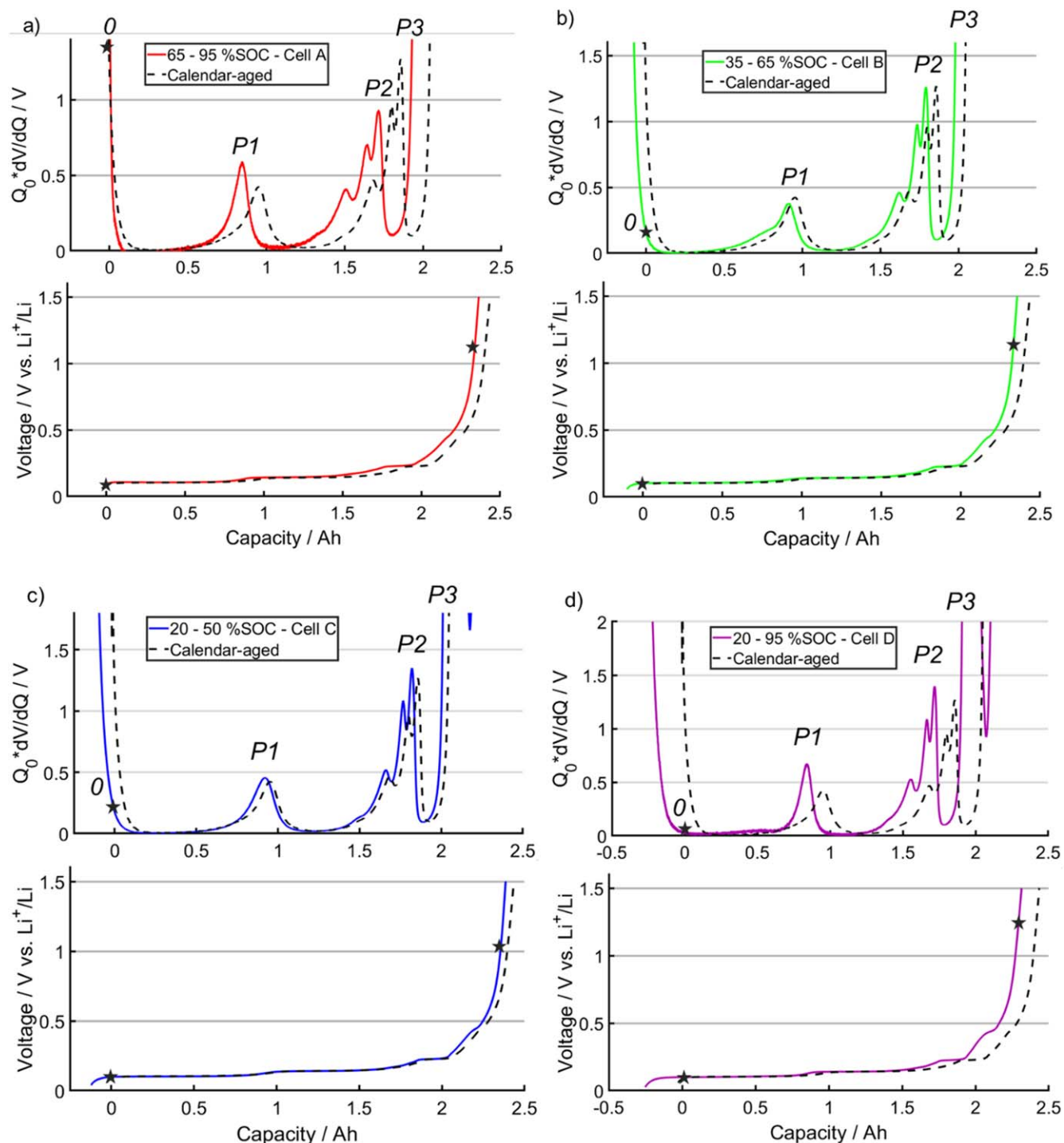


Figure 5. Deintercalation curves and their respective differential voltage curves of graphite/lithium half-cells, harvested from cells A (a), B (b), C (c), D (d) and calendar-aged for comparison (dashed line). The black stars mark where the discharge process starts and ends, corresponding to the full-cell voltage cut-off points.

degradation rate is considerably reduced, incrementing its lifetime. Additionally, calendar-aging effects are considered due to the low *c*-rate cycling and long periods of resting, including the unexpected ones.^{18,23} Although cells were cycled at mild temperature (25 °C), high cut-off voltages trigger secondary reactions in both electrodes,^{9,31} which cause capacity fade and also increase of cell impedance.

Electrochemical impedance spectroscopy of cylindrical cells.—

Figure 2 shows the impedance spectra at EOT for four cells cycled

under the four different cycling procedures, a calendar-aged cell is shown as comparison. Electrochemical impedance spectroscopy (EIS) characterization was performed at 50% SOC and 25 °C in each case. Both cells B and C present similar arc shapes with no significant changes compared to the calendar-aged cell. However, an increment in the ohmic resistance at high frequencies (1 kHz) was observed, and the length of the depressed semicircle is slightly larger than for the calendar-aged cell. Increase in the semicircle length is typically associated with the impedance from superficial phenomena at the electrode/electrolyte interface in both electrodes.³² The spectra

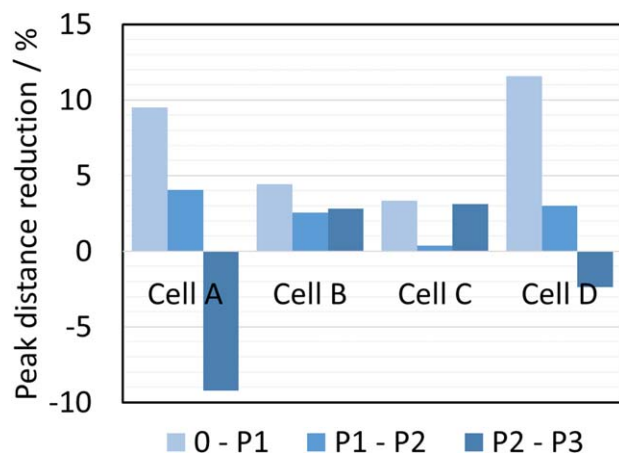


Figure 6. Peak distance reduction of graphite half-cells DV curves relative to the calendar-aged electrode.

of cell A, which was cycled with higher cut-off voltages and narrow Δ SOC, presents a relatively large-arc semicircle and the development of a secondary semicircle is observed at middle frequencies (10 Hz), compared to calendar-aged cell. Finally, Cell D, which was cycled with high cut-off voltages and wide Δ SOC, presents the largest impedance increase, and the development of a secondary semicircle as well.

The low-frequency reactance minimum points decreased from 3.2 Hz for the calendar-aged cell to 0.6, 1.6, and 0.5 Hz for cells A, B, and D respectively, whereas it was maintained by cell C at 3.2 Hz. On the other hand, the high-frequency limit is shifted slightly from 13.6 m Ω to 14.3, 14.0, 14.0, and 14.1 m Ω for cells A, B, C, and D, respectively. This is a sign of the slowing down of the cell processes due to aging.³²

The development of a secondary semicircle observed in Fig. 2 for cells A and D has been reported in literature for NCA/graphite cells.³³ The resistance increase of the electrode/electrolyte interface could be related to the SEI growth on the graphite surface but also to the particle cracks and particle-surface micro-cracks.^{6,9}

Individual electrode loss of capacity analysis and cell balance.—Capacity loss is generally caused by two main aging mechanisms, loss of lithium inventory (LLI) and loss of active material (LAM).^{19,34,35} In order to differentiate them from the total capacity loss observed above, it is necessary to evaluate the capacity loss of each electrode from each cell and compare it to a reference, which in this case is the calendar-aged cell. Therefore, *post-mortem* analysis of each electrode was performed to evaluate the capacity loss mode.

Graphite electrode.—Figure 3 shows the voltage vs capacity relationship during the deintercalation process for graphite/lithium half-cells, using electrodes collected from cycle-aged and calendar-

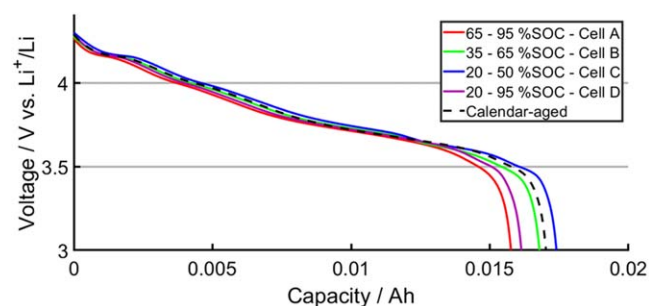


Figure 7. Discharge curves of the NCA electrode harvested from cells A, B, C, and D and calendar-aged cell (dashed line).

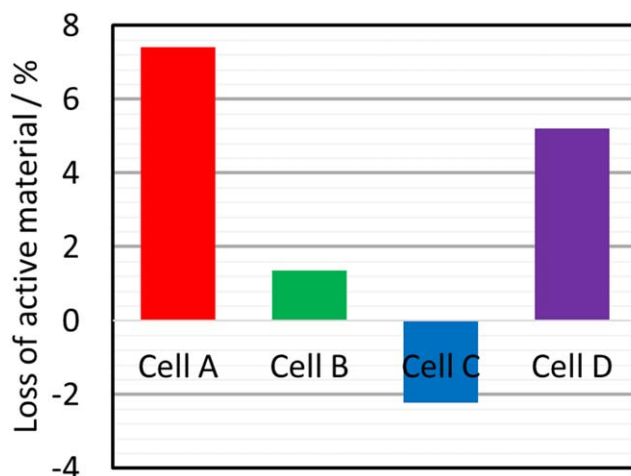


Figure 8. Loss of active material of NCA/lithium cycled-aged half-cells relative to calendar-aged half-cell, after partial cycling at different SOC ranges.

aged full-cells. At the end of the deintercalation curve (1.5 V), we can observe that curves of the cycle-aged half-cells are shifted to the left relative to the calendar-aged half-cell. Cell A presents the largest shift followed by cells D, B and C, in that order.

It is possible to calculate the amount of capacity that each electrode from cycle-aged cells has lost by comparing them to the calendar-aged cell. The capacity loss accounted as LAM is caused by the cycling regime of each cell. Figure 4 shows the LAM percentage from the graphite electrode of each cycle-aged cell relative to the calendar-aged graphite electrode. We can observe that cell A presents the greatest LAM percentage relative to the calendar-aged cell with 12.6%, whereas cells B, C and D present smaller values, 2.3, 0.6 and 3.0%, respectively.

For a further detailed analysis, differential voltage analysis (DVA) is used to gain insights of the capacity loss mechanisms at the graphite electrode. Graphite as electrode material for LIBs has been studied using DVA by many authors.^{36–41} Figure 5 shows the DV curves along with the discharge curves for each cycle-aged cell. Among the peaks displayed in Fig. 5, in this work, we are going to quantify the capacity delivered by the stages between the marked peaks. The marks in Fig. 5 represent the starting point (0), peak 1 (P1), peak 2 (P2), and peak 3 (P3), corresponding to the deintercalation process. Distances between marked peaks can be quantified and then compared to those obtained from the calendar-aged electrode. The peaks correspond to phase transitions that are characteristic for the graphite electrode.⁴² The black stars on the discharge curves mark where the deintercalation process starts and ends, corresponding to the full-cell voltage cut-off points. Peak shifting towards negative capacities are related to the LLI, whereas changes in the distance between peaks indicate the effect of LAM.^{43,40} The LLI caused by secondary reactions can be identified by observing the shift towards negative capacity in Fig. 5. Cells B, C, and D clearly present this shift, whereas cell A does not.

In order to obtain the curves from Fig. 5, discharge curve data from half-cells needs to be fitted to the full-cell discharge curve. The x-axis capacity values have been scaled and the discharge curves shifted along the x-axis for each electrode. The voltage fitting method is presented in detail by Honkura et al.^{34,44} and was further developed by Mussa et al.²⁷ and Svens et al.⁴⁵ After the fitting procedure it is possible to quantify LAM and LLI for each electrode.

Figure 6 shows that for cells A and D, peak distance 0—P1 has been reduced to a greater extent than in cells B and C. Accordingly, the capacity available in the first deintercalation phase, compared to the calendar-aged cell, has been reduced 9.5, 4.4, 3.3, and 11.3% for cells A, B, C, and D, respectively. These results are in accordance

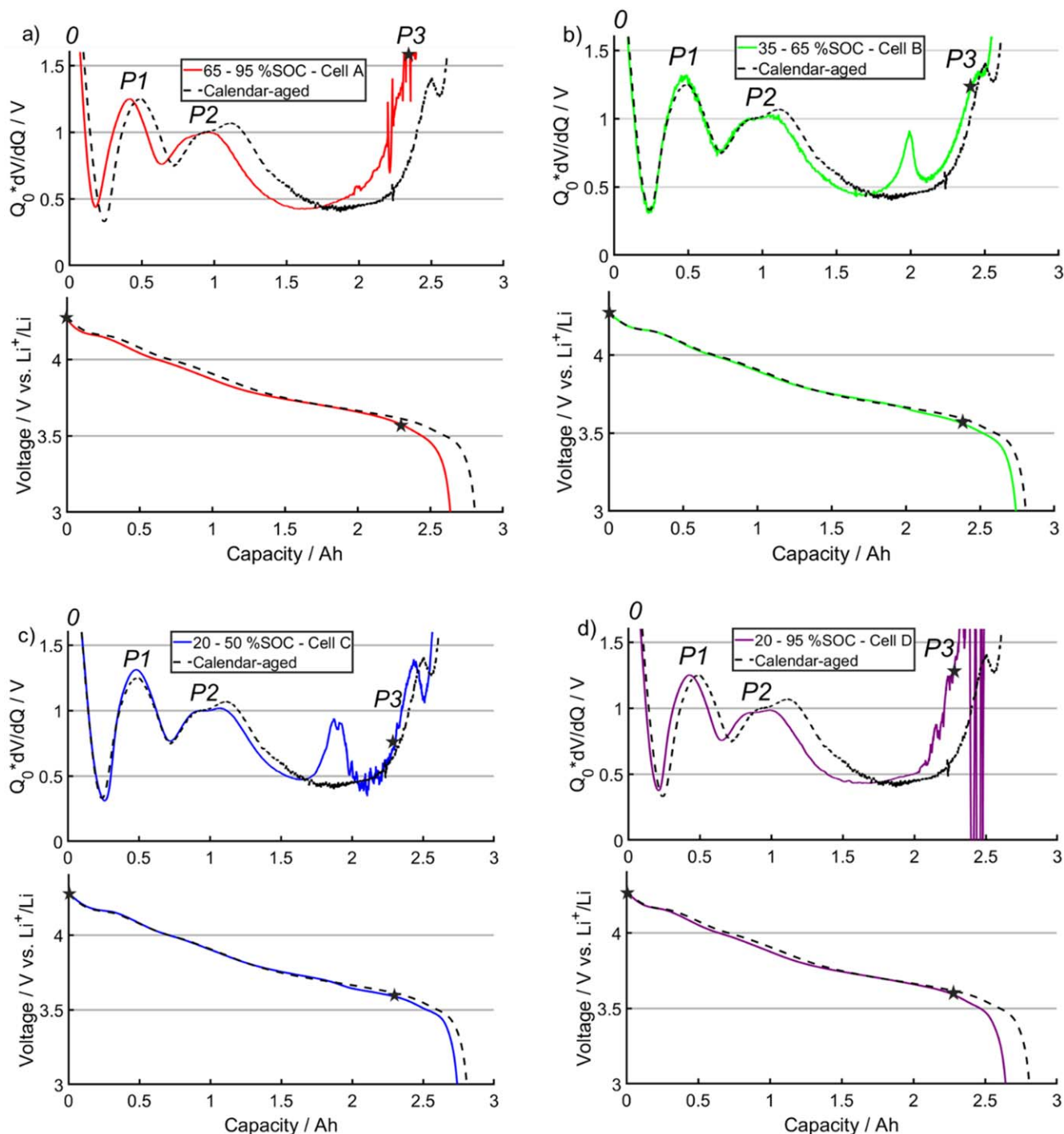


Figure 9. Intercalation curves and their respective differential voltage curves of NCA/lithium half-cells, harvested from cells A (a), B (b), C (c), D (d) and calendar-aged for comparison, as black dashed lines. The black stars mark where the discharge process starts and ends, corresponding to the full-cell voltage cut-off points.

with those presented for full-cell capacity loss (Fig. 1). Furthermore, peak P1 height increases for cells A and D (Figs. 5a, 5d), and the change is less evident for cells B and C (Figs. 5b, 5c). This seems to correspond to the impedance increase observed in Fig. 2. Peak distance P1–P2 represents the second deintercalation stage where cells A, B, and D present considerable capacity losses of 4.0, 2.5, and 2.9%, respectively, and cell C presents a relatively small value of 0.3%. Finally, peak distance P2–P3 represents the last deintercalation stage, where cells A and D present capacity gains of 9.2 and 2.3%, respectively, while cells B and C present capacity losses of 2.8

and 3.1%, respectively. A gain in capacity is observed in cells which have been cycled around high voltages and corresponds to the region of high potential for the graphite electrode. This may be evidence of capacity recovery as was pointed out in Fig. 1.

NCA electrode.—Figure 7 shows the voltage-capacity curves for the lithiation process of NCA/lithium half-cells. NCA electrodes were collected from cycle-aged full-cells and a calendar-aged full-cell as reference. The LAM of each cycle-aged electrode is evaluated by comparing it to the non-cycled calendar-aged cell electrode.

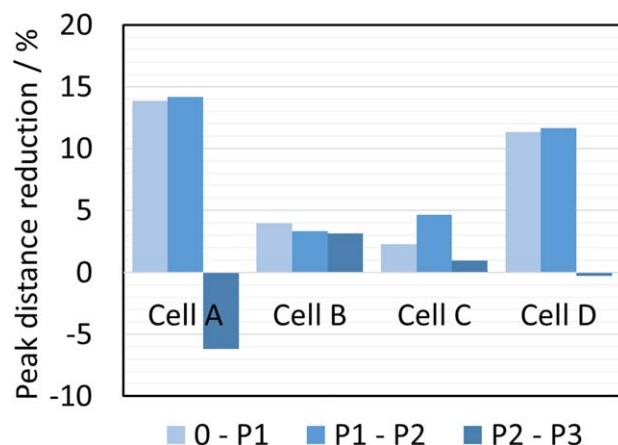


Figure 10. Peak distance reduction of NCA half-cell DV curves relative to the calendar-aged electrode.

A quantification of LAM is presented in Fig. 8. Cells A and D present the greatest capacity losses with 7.4 and 5.2%, respectively. Although cell B shows less capacity loss with 1.4%, Cell C presents a gain in capacity of 2.2% relative to the calendar-aged cell.

As with the graphite electrode, DVA was used to evaluate NCA/lithium half-cells and gain insight to the loss of capacity mechanisms. NCA/lithium presents three main peaks associated to three characteristic phase transitions in the NCA material.^{21,46–49} Figure 9 presents DV curves and corresponding discharge curves for each cycle-aged cell. The peak distance is measured between the marked points: starting point (0), peak 1 (P1), peak 2 (P2), and peak 3 (P3), corresponding to the intercalation process. Each set of data from half-cell discharge curves went through the voltage fitting procedure to match the full-cell discharge curve; the black star shows the full-cell low voltage cut-off point.

In Fig. 10 we evaluate the reduction between peaks distances to gain insights of capacity loss modes. Peak distance 0–P1 represents the intercalation stage at the electrode high potential region. Cells A and D show greater peak distance reduction relative to the calendar-aged cell, 13.8 and 11.3%, respectively, whereas cells B and C present lower values, 3.9 and 2.3%, respectively. Correlation between cycling at high voltages and capacity loss is evident. Peak distance reduction between P1 and P2 follows the same trend, cells A and D show greater reduction, 14.2 and 11.6%, respectively, while cells B and C show reductions of 3.3 and 4.6%, respectively. Finally, peak distance P2–P3, which is the largest intercalation stage at the electrode middle to low potential region, shows the opposite trend. Cells A and D show gains of capacity of 6.2 and 0.2%, respectively, whereas cells B and C show losses of capacity of 3.1 and 0.9%, respectively. An unexpected peak is observed only in cells B and C around 1.87 Ah, it is believed to be an artifact caused by cell disassembling, material handling and/or half-cell preparation. After the voltage fitting procedure, no significant shift of the electrodes towards negative capacities is observed, indicative of minimal LLI. Therefore, the main capacity loss mechanism for the NCA electrode is LAM. We also observe a correlation between LAM and cycling at high voltages, which can be explained by the mechanical stress associated to intercalation/deintercalation processes and phase transition in the NCA material.⁵⁰ Moreover, the generation of micro-cracks in the surface of the particles, which is believed to be due to the formation of a new surface phase (NiO-type), can be another cause of LAM in NCA electrodes.^{5,12}

SEM analysis.—SEM images of NCA and graphite electrodes collected from cycle-aged and calendar-aged full-cells are shown in Fig. 11.

Differences were observed in NCA particles between cycle-aged and calendar-aged electrodes. NCA electrode samples show NCA

primary particles agglomerated into secondary particles, presumably using PVDF binder, with carbon black dispersed on the surface of the secondary particles to enhance electronic conduction. Cycle-aged primary particles present signs of deagglomeration cracks (red arrows). Samples from cells A and D, Figs. 11a and 11b respectively, are mainly affected by particle cracking. Some particles also present micro-cracks on their surface and deagglomeration is observed with some cases of complete particle isolation. Although samples from cells B and C present deagglomeration of primary particles, the signs of particle cracking are less evident. From Fig. 11e, primary particles in the sample from a calendar-aged cell show highly compact agglomeration to form secondary particles and no evidence of cracks in the surfaces of primary particles is observed.

From EDX analyses we observed that the graphite electrode contains some graphite agglomerations coated with a silicon-based compound, containing 1% silicon atomic percentage. Following cycling, the silicon yolk-shield structure was observed to crack and cause delamination of the graphite flake agglomeration contained inside. In the case of samples from cells A and D, the cracks are evident and observable with SEM, Figs. 11f–11i. The silicon-based yolk-shield surface seems to have an amorphous, rough morphology with large surface area.

Figures 11f–11j shows SEM images from harvested graphite electrodes. They are mainly composed of agglomerations of graphite flakes stacked on top of each other, and EDX analyses show coatings with silicon-based compound covering some particles in a yolk-shield structure. Graphite particle cracking is only observed in a sample from cell D, whereas cracks in the yolk-shield structure are observed in samples from cells A, B and C. A sample from a calendar-aged cell shows no evidence of cracks in the silicon yolk-shield nor in graphite particles whatsoever. Cracks in the silicon yolk-shield could be potentially caused by cycle-aging processes and are observed in large extent for samples cycled at high cut-off voltages and narrow and wide Δ SOC.

Conclusions

In the present work we propose a new protocol for testing and studying the aging mechanisms of NCA/graphite lithium-ion batteries applied in off-grid PV-systems. Long-term, low c-rate and various state of charge ranges (Δ SOC) are characteristics of those applications and therefore the aging protocols. Using low c-rate and high cut-off voltages will cause material degradation of the NCA electrode and cell impedance increase. However, it is not wide Δ SOC but a combination of narrow Δ SOC and high cut-off voltage that largely deteriorate the cell.

Differential voltage analysis was performed on half-cells with NCA/lithium and graphite/lithium to analyze loss of active material and shift of the electrodes. A strong dependency between material degradation at high cut-off voltages and impedance increase was observed. Cells cycled over wide Δ SOC showed a larger impedance increase than the ones cycled in narrow Δ SOC, although both present the formation of a second semicircle in Nyquist impedance plots. This can be attribute to the observed larger graphite electrode shift for the wide Δ SOC case.

An unexpected gain in capacity is observed from in-depth DVA peak analysis in the cell cycled at low cut-off voltage and narrow Δ SOC. Although major capacity fade is observed from cells cycled with high cut-off voltages and narrow Δ SOC, DVA peak analysis revealed a gain in capacity in the last stage of lithium deintercalation from the graphite electrode. Likewise, the same behavior was observed for the NCA electrode in the last lithium intercalation stage. On the other hand, a large capacity loss is observed in the first stage of deintercalation and lithiation for the graphite and NCA electrodes, respectively. Images from SEM confirm the findings of material degradation at high cut-off voltages. A considerable amount of primary particle cracking and deagglomeration from secondary

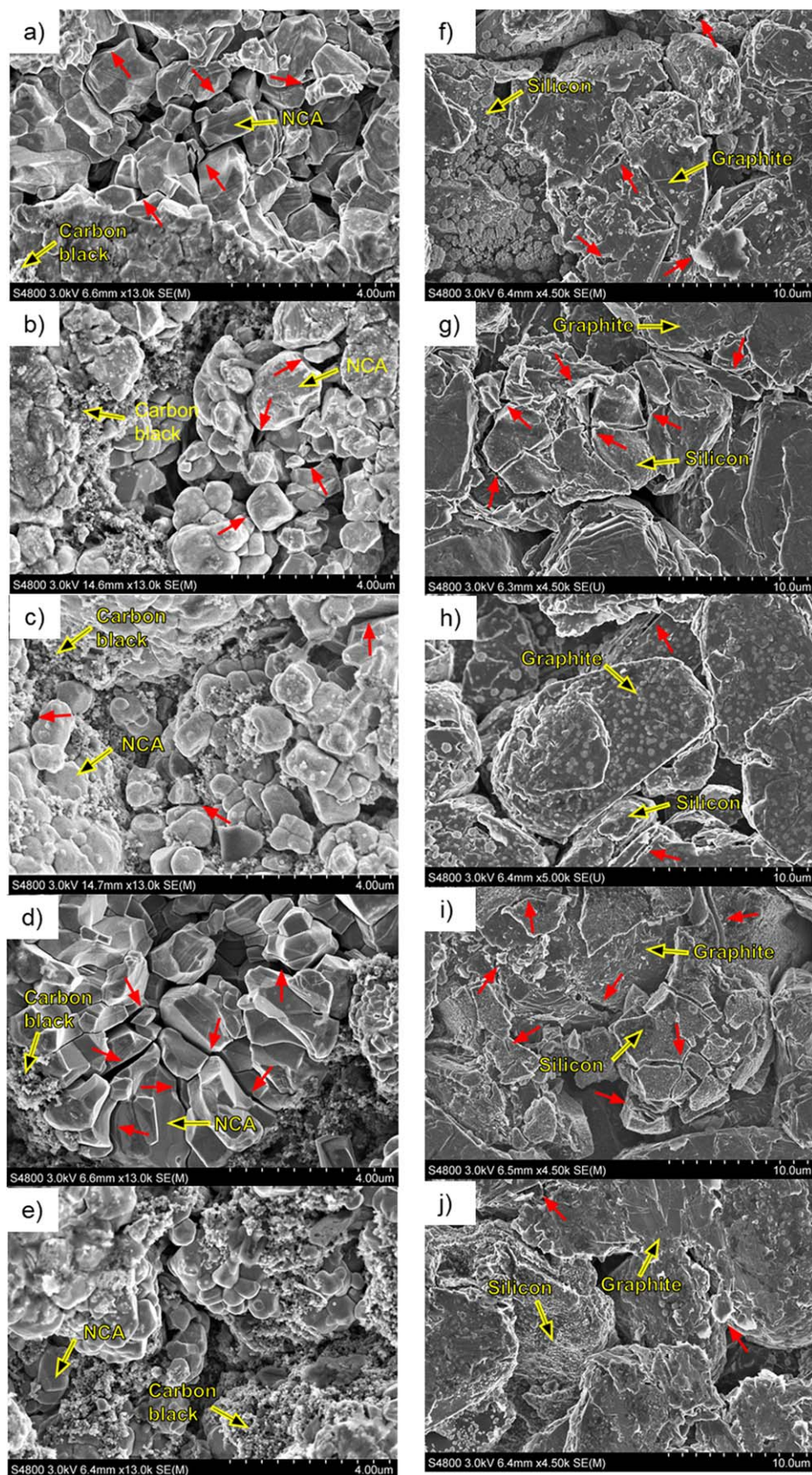


Figure 11. SEM images of NCA (a)–(e) and graphite (f)–(j) electrodes samples: (a), (f) cell A, (b), (g) cell B, (c), (h) cell C, (d), (i) cell D, and (e), (j) calendar-aged cell. Red arrows indicate cracks on primary and secondary particles on NCA electrode samples, and cracks on silicon yolk-shell and delamination of graphite primary particles.

particles is observed in the NCA electrode sample, while cracks and expansion of the silicon-compound yolk-shell structure have caused delamination of some graphite particle flakes.

The combination of narrow Δ SOC and middle to low cut-off voltages shows a moderate to low degradation effect. More importantly, under realistic conditions of low c-rate cycling, cell

deterioration is greatly reduced for low and middle cut-off voltages, increasing the cell lifetime enough to avoid replacement in applications with long lifetime requirements.

Acknowledgments

The financial support of the Swedish International Development Cooperation Agency (SIDA) is gratefully acknowledged.

ORCID

Fabian Benavente-Araoz  <https://orcid.org/0000-0003-1878-1530>

Maria Varini  <https://orcid.org/0000-0002-8532-122X>

Anders Lundblad  <https://orcid.org/0000-0002-1226-0788>

Saúl Cabrera  <https://orcid.org/0000-0001-5339-4080>

Göran Lindbergh  <https://orcid.org/0000-0001-9203-9313>

References

1. F. Benavente et al., *Appl. Energy*, **235**, 519 (2019).
2. S. Bourlot, P. Blanchard, and S. Robert, *J. Power Sources*, **196**, 6841 (2011).
3. S. Watanabe, M. Kinoshita, T. Hosokawa, and K. Morigaki, *J. Power Sources*, **260**, 50 (2014).
4. S. Muto et al., *J. Electrochem. Soc.*, **156**, 371 (2009).
5. D. P. Abraham, E. M. Reynolds, E. Sammann, A. N. Jansen, and D. W. Dees, *Electrochim. Acta*, **51**, 502 (2005).
6. S. Watanabe, M. Kinoshita, and K. Nakura, *J. Power Sources*, **247**, 412 (2014).
7. I. Bloom, J. P. Christophersen, D. P. Abraham, and K. L. Gering, *J. Power Sources*, **157**, 537 (2006).
8. K. Darcovich, E. R. Henquin, B. Kenney, I. J. Davidson, and N. Saldanha, *Appl. Energy*, **111**, 853 (2013).
9. Y. Mao et al., *Adv. Funct. Mater.*, **29**, 1 (2019).
10. P. Zhou et al., *J. Mater. Chem. A*, **5**, 2724 (2017).
11. I. Bloom et al., *J. Pow. Sour.*, **195**, 877 (2010).
12. S. Watanabe, T. Hosokawa, K. Morigaki, M. Kinoshita, and K. Nakura, *ECS Transactions*, **41**, 65 (2012).
13. S. Watanabe, M. Kinoshita, and K. Nakura, *J. Power Sources*, **196**, 6906 (2011).
14. D. Mohanty et al., *Sci. Rep.*, **6**, 1 (2016).
15. P. Kalyani and N. Kalaiselvi, *Sci. Technol. Adv. Mater.*, **6**, 689 (2005).
16. K. Du et al., *ACS Appl. Mater. Interfaces*, **8**, 17713 (2016).
17. X. Li et al., *Electrochim. Acta*, **174**, 1122 (2015).
18. P. Keil et al., *J. Electrochem. Soc.*, **163**, 1872 (2016).
19. P. Keil and A. Jossen, *J. Electrochem. Soc.*, **164**, 6066 (2017).
20. H. H. Ryu, K. J. Park, C. S. Yoon, and Y. K. Sun, *Chem. Mater.*, **30**, 1155 (2018).
21. B. Huang, X. Li, Z. Wang, H. Guo, and X. Xiong, *Ceram. Int.*, **40**, 13223 (2014).
22. G. Zhao, W. Wu, W. Qiu, S. Liu, and G. Wang, *Scientific. Net.*, **528**, 202 (2012), <https://www.scientific.net/AMR.528.202>.
23. A. J. Smith, H. M. Dahn, J. C. Burns, and J. R. Dahn, *J. Electrochem. Soc.*, **159**, 2 (2012).
24. J. Li et al., *J. Electrochem. Soc.*, **165**, A2682 (2018).
25. J. E. Harlow et al., *J. Electrochem. Soc.*, **166**, A3031 (2019).
26. F. Benavente-Araoz et al., *Energy Procedia*, **142**, 3715 (2017).
27. A. S. Mussa, M. Klett, M. Behm, G. Lindbergh, and R. W. Lindström, *J. Energy Storage*, **13**, 325 (2017).
28. A. Eddahech, O. Briat, and J. M. Vinassa, *Electrochim. Acta*, **114**, 750 (2013).
29. M. Lewerenz, P. Dechent, and D. U. Sauer, *J. Energy Storage*, **21**, 680 (2019).
30. S. Watanabe, M. Kinoshita, T. Hosokawa, and K. Morigaki, *J. Power Sources*, **258**, 210 (2014).
31. C. R. Birkel, M. R. Roberts, E. Mcturk, P. G. Bruce, and D. A. Howey, *J. Power Sources*, **341**, 373 (2017).
32. D. P. Abraham, J. L. Knuth, D. W. Dees, I. Bloom, and J. P. Christophersen, *J. Power Sources*, **170**, 465 (2007).
33. S. Gantenbein, M. Weiss, and E. Ivers-ti, *J. Power. Sources.*, **379**, 317 (2018).
34. K. Honkura, K. Takahashi, and T. Horiba, *J. Power Sources*, **196**, 10141 (2011).
35. B. Stiaszny et al., *J. Power Sources*, **258**, 61 (2014).
36. M. Dubarry and B. Y. Liaw, *J. Power. Sources.*, **194**, 541 (2009).
37. P. Liu et al., *J. Electrochem. Soc.*, **157** (2010).
38. M. Dubarry, C. Truchot, and B. Y. Liaw, *J. Power Sources*, **258**, 408 (2014).
39. M. Safari and C. Delacourt, *J. Electrochem. Soc.*, **158**, A1123 (2011).
40. M. Dubarry, C. Truchot, and B. Y. Liaw, *J. of Power Sources*, **219**, 204 (2012).
41. X. Han, M. Ouyang, L. Lu, and J. Li, *J. Power Sources*, **268**, 658 (2014).
42. E. Sarasketa-Zabala et al., *J. Phys. Chem. C*, **119**, 896 (2015).
43. C. Pastor-fern, K. Uddin, G. H. Chouchelamane, W. D. Widanage, and J. Marco, *J. Power Sources*, **360**, 301 (2017).
44. K. Honkura and T. Horiba, *J. Power Sources*, **264**, 140 (2014).
45. P. Svens et al., *J. Power Sources*, **270**, 131 (2014).
46. K. Kleiner et al., *J. Power. Sources.*, **273**, 70 (2015).
47. J. Shim and K. A. Striebel, *J. Power. Sources.*, **122**, 188 (2003).
48. L. Zhang, J. Fu, and C. Zhang, *Nanoscale Res. Lett.*, **12**, 1 (2017).
49. P. Xiao, T. Lv, X. Chen, and C. Chang, *Sci. Rep.*, **1** (2017).
50. J. Vetter, P. Nov, M. R. Wagner, and C. Veit, *J. Power. Sources.*, **147**, 1 (2005).
51. M. Lang et al., *J. Power Sources*, **326**, 397 (2016).